

Erosion–corrosion behavior of SAF3207 hyper-duplex stainless steel

Hong-liang Xiang^{1,2)}, Yu-rui Hu¹⁾, Hua-tang Cao³⁾, Dong Liu¹⁾, and Xuan-pu Dong⁴⁾

1) School of Mechanical Engineering and Automation, Fuzhou University, Fuzhou 350108, China

2) Jinjiang Science and Education Park, Fuzhou University, Jinjiang 362251, China

3) Department of Advanced Production Engineering, Engineering and Technology Institute Groningen, University of Groningen, Nijenborgh 4, 9747AG, The Netherlands

4) State Key Laboratory of Materials Processing and Die & Mould Technology, Huazhong University of Science and Technology, Wuhan 430074, China

(Received: 16 May 2019; revised: 28 July 2019; accepted: 31 July 2019)

Abstract: Polarization curves and mass losses of SAF3207 hyper-duplex stainless steel under various conditions were measured. The damaged surfaces after erosion–corrosion tests were characterized by scanning electron microscopy. The results showed that an increase in flow velocity could enhance the electrochemical corrosion and consequently decrease the passivation properties of the steel. The erosion–corrosion damage of the samples increased substantially when the flow velocity exceeded the critical value of $4 \text{ m}\cdot\text{s}^{-1}$. The mass loss rate increased as the sand content increased, reaching a maximum at 7wt% sand content, corresponding to the most severe electrochemical corrosion damage. When the sand content was increased further, however, the mass loss rate decreased and then tended stable. The mass loss was divided into incubation, sustained, and stationary periods, with a maximum mass loss rate of $12.97 \text{ g}\cdot\text{h}^{-1}\cdot\text{m}^{-2}$ after an erosion period of 2.5 h. The erosion–corrosion mechanism was investigated in detail.

Keywords: hyper duplex stainless steel; erosion corrosion; flow velocity; electrochemical corrosion; microstructure morphology

1. Introduction

Erosion–corrosion, which is the phenomenon of surface degradation of a material subjected to a high-speed relative motion of a corrosion fluid, becomes significant in liquid–solid flow systems. Numerous studies [1–6] have reported that the combined effects of erosion and corrosion accelerate the material loss in a flow system, inducing a remarkable mass loss compared with the effect caused by erosion or corrosion individually. In fact, erosion–corrosion is a complex process affected by numerous factors [7], including the concentration, temperature, pH value, and oxygen capacity of the corrosive media; the concentration of active ions; the particle size, hardness, and shape of the solid phase; and the chemical composition, microstructure, mechanical properties, and corrosion resistance of the tested material.

Because of their excellent corrosion resistance, high strength, and high durability, the duplex stainless steels are widely used in the petroleum chemical industry, shipbuilding, bridge construction, underwater pipelines, and me-

chanical parts [8]. As newly developed stainless steels suitable for use in a wide range of marine applications [9–10], the SAF3207 hyper-duplex stainless steels exhibit superior corrosion resistance and mechanical properties compared with other types of stainless steels. However, thus far, reports on the corrosion behavior of the SAF3207 hyper-duplex stainless steels have been limited. In the present work, the effects of velocity, sand content, and time on the slurry erosion–corrosion of SAF3207 hyper-duplex stainless steels were studied using a homemade erosion tester. The failure mechanism of this material was investigated.

2. Experimental

The experimental steel was prepared using a high-frequency induction furnace made of 316L stainless steel, molybdenum iron, electrolytic chromium, electrolytic manganese, and a nitride alloy. The chemical composition of the experimental steel was determined by an optical emission spectrometer as listed in Table 1.

Table 1. Chemical composition of SAF3207 steel wt%

C	Si	P	S	Mn	Cr	Ni	Mo	N	Fe
0.021	0.62	0.023	0.013	0.74	33.27	7.02	3.49	0.72	Bal.

The pitting resistance equivalent value was 56.74 (greater than 48), indicating the steel meets the chemical composition of the SAF3207 super duplex stainless steel. The cast ingots were solid-solution treated in a KSS-1700 box resistance furnace. The solution treatment was carried out at 1200°C for 2 h, followed by water cooling.

The erosion–corrosion experiments were performed with a slurry wear apparatus. The reference electrode was a saturated calomel electrode and the auxiliary electrodes (AE) were platinum electrodes. Both were placed in the slurry jar and connected to an electrochemical workstation, as shown in Fig. 1. The electrochemical working electrodes and mass samples were attached to the rotating disk with an impact angle of 0°.

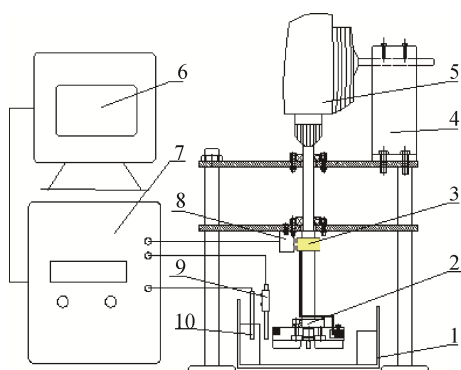


Fig. 1. Schematic of the erosion–corrosion tester. 1—Slurry jar; 2—Rotating disk; 3—Copper ring; 4—Support; 5—Motor; 6—Personal computer; 7—Electrochemical workstation; 8—Copper brush; 9—Auxiliary electrode; 10—Reference electrode.

The electrochemical measurements were conducted on a CH Instruments CHI650C workstation. The potential of the working electrode was set to vary from –800 to 1200 mV at a scanning rate of 0.5 mV·s⁻¹. The working size of the electrochemical test specimens was 6 mm × 6 mm. The non-working face was sealed with epoxy. A copper wire was utilized for the specimen and for the copper ring connection from the rear of the specimen. Medium solutions with different sediment contents were prepared using garnet sand and 3.5wt% NaCl. The grain size of the garnet sand was approximately 60 mesh. Fig. 2 shows the morphology of the garnet sand used in the experiments. The erosion–corrosion potentiodynamic polarization of the SAF3207 hyper-duplex stainless steel was measured under an impinging jet of a so-

lution of 3.5wt% NaCl + 5wt% sand at various velocities (0–8 m·s⁻¹). Also, the velocity was controlled by the rotation rate of the disk. The erosion–corrosion behaviors of the samples were studied by varying the medium garnet sand content from 2wt% to 11wt% in a 3.5wt% NaCl solution. The velocity was set at 6 m·s⁻¹, and the testing duration was 2 h. The microhardness was measured by a MVC-1000D1 microhardness tester.

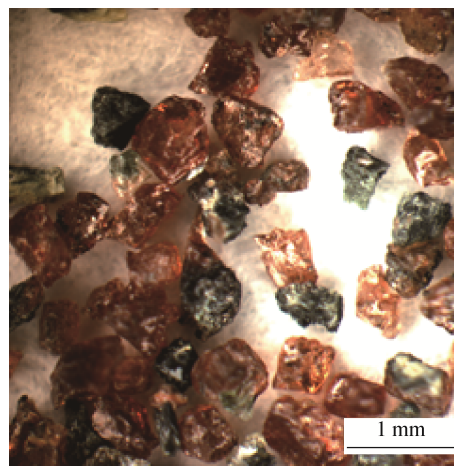


Fig. 2. Micrograph of the garnet sand used in the experiments.

The size of the weightlessness specimens was 10 mm × 14 mm. The specimens were weighed before and after the experiments using an electronic balance with a precision of 0.1 mg. The mass loss rate could be expressed by the following equation:

$$W = \frac{\Delta m}{S \cdot t} \quad (1)$$

where W is the wear rate, g·h⁻¹·m⁻²; Δm is the mass loss, g; S is the area of the working surface, m²; and t is the duration, h. The final deterioration rate was determined by averaging the test results for three samples. The specimens used in the erosion–corrosion tests were subsequently observed by scanning electron microscopy (SEM) operating at 10 kV.

3. Results and discussion

3.1. Effect of velocity

The erosion–corrosion potentiodynamic polarization of the SAF3207 hyper-duplex stainless steel was measured under an impinging jet of a solution of 3.5wt% NaCl + 5wt% sand at various velocities (0–8 m·s⁻¹). Also, the velocity was controlled by the rotation rate of the disk. The erosion results (Fig. 3) show that, at the velocity of 0 m·s⁻¹, the polarization curve could be divided into three zones: the

active–passive transition zone (section *b–c* in Fig. 3), the passive zone (section *c–d* in Fig. 3), and the transpassive zone (the section after point *d* in Fig. 3). For velocities greater than $0 \text{ m}\cdot\text{s}^{-1}$, all curves demonstrate the same tendency; however, no substantial active–passive transition was observed [11]. In addition, the corrosion potentials of the samples under the investigated velocities ($0\text{--}8 \text{ m}\cdot\text{s}^{-1}$) of sand erosion were clearly passively shifted compared with that of the sample without erosion ($0 \text{ m}\cdot\text{s}^{-1}$).

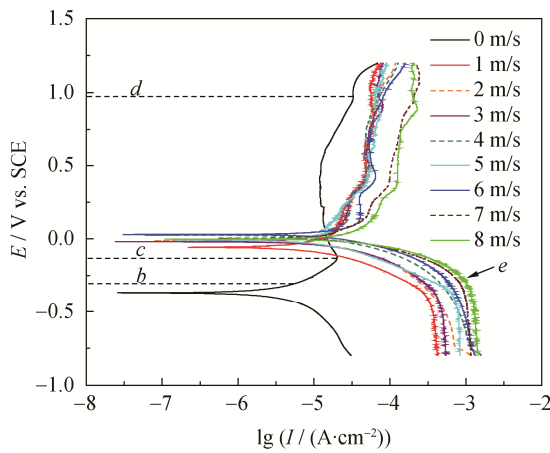


Fig. 3. Polarization curves of specimens at various flow velocities (*E*—potential; *I*—current density).

To obtain an in-depth understanding of the electrochemical reaction, an electrochemical workstation with the CHI650C software was used to fit the parameters of the potentiodynamic curves under various velocities; the results are presented in Table 2.

Table 2. Test parameters of potentiodynamic curves

Velocity / ($\text{m}\cdot\text{s}^{-1}$)	I_d / ($\mu\text{A}\cdot\text{cm}^{-2}$)	E_{corr} / V	I_p / ($\mu\text{A}\cdot\text{cm}^{-2}$)
0	20	-0.368	12.589
1	316	-0.021	30.128
2	331	-0.011	31.622
3	378	0.015	32.118
4	562	0.022	35.481
5	771	0.026	38.265
6	892	0.028	39.811
7	987	0.029	100.712
8	1122	0.031	125.892

Note: I_d —diffusion current density; E_{corr} —corrosion potential; I_p —passive current density.

According to Table 2, the diffusion current density I_d (current density value at point *e* in Fig. 3) increased with increasing flow velocity. This increase in diffusion current density occurred because the samples underwent oxy-

gen-absorption corrosion with oxygen as the depolarizing agent in a 3.5wt% NaCl solution, whereas the oxygen transferring onto the metal surface was the dominant process in the cathode reaction [12]. The diffusion current density I_d [13] could be estimated from the Nemst–Fich equation:

$$I_d = \frac{\eta f D_{\text{O}_2} [\text{O}_2]}{\delta} \quad (2)$$

where I_d is the diffusion current density, f is the Faraday constant, D_{O_2} and $[\text{O}_2]$ are the diffusion coefficient and oxygen concentration in the solution, respectively, n is the number of reaction electrons, and δ is the diffusion layer thickness.

Therefore, on the one hand, the increase in velocity increased the oxygen concentration in the solution; on the other hand, it might also reduce the thickness of the metal solution diffusion layer δ , enabling a greater amount of oxygen to easily penetrate the diffusion layer and reach the metal surface for reaction, thereby increasing the diffusion current density I_d . Table 2 also demonstrates that the corrosion potential E_{corr} increased with increasing flow velocity. The main reason for this behavior is that the corrosion potential was proportional to the oxygen concentration in the solution but inversely proportional to the thickness of the diffusion layer. Thus, the changes in the corrosion potential E_{corr} and diffusion current density I_d reflect the changes of the flow velocity.

In Table 2, the passive current density I_p (current density value in section *c–d* in Fig. 3) at fluidization is apparently greater than the passive current density at the static state and it increased with increasing flow velocity. Xiang *et al.* [14] discovered that a passive film with excellent corrosion resistance was formed in the passive zone and that the passive film sustained constant dissolution and dynamically repaired itself during the same process. The higher the dissolution and repairing rates, the greater the I_p and the worse the passivation performance would be. From the experimental results, we inferred that the passivation performance of samples under the dynamic flushing condition was poorer than the passivation performance of samples under the static condition. The greater the flow velocity, the poorer the passivation performance. We attributed this behavior to the high-speed liquid–solid flow reducing the thickness of the passivation film, inducing rapid dissolution and consequently triggering substantial damage to the passivation film.

The mass loss rate curves of the specimens under various flow velocities are presented in Fig. 4. The velocities were the same as those previously mentioned, and the test duration was 2 h.

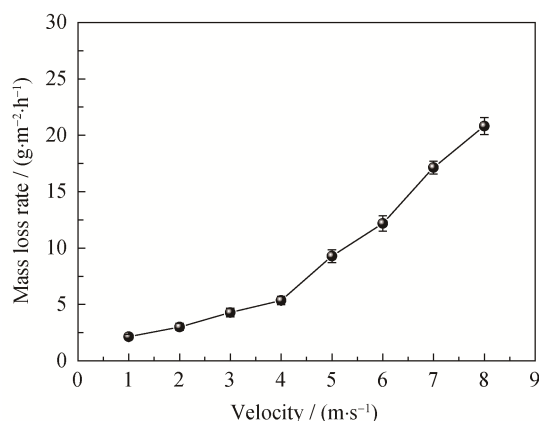


Fig. 4. Mass loss rate curve of specimens at various flow velocities.

Fig. 4 shows that the mass loss rate increased as the flow velocity increased. This behavior is attributed to two reasons: First, the mixing at a higher speed generated a greater number of bubbles. Huang [15] proposed that the broken bubbles on the surface induce instant shockwaves and lead to cavitation erosion. Continuous cavitation erosion would cause fatigue failure or even surface denudation of the samples. In the present work, however, the period for testing was not sufficient to produce enough bubbles to induce this shockwave effect. Second, the total dynamic energy of the sand increased along with the flow velocity, thereby increasing the force on the surface and accelerating the corrosion [16]. This effect was the main reason for the mass loss in the present work.

The critical velocity has been proposed as a value below which the mass loss rate increases gently, whereas at velocities greater than the critical velocity, the mass loss rate of the materials increases dramatically [17–18]. Different values for the critical velocity were obtained in previous studies because of the various materials and experimental methods used. In the present work, when the velocity was less than 4 m·s⁻¹, the mass loss rate increased slowly. However, the rate increased substantially when the velocity was increased beyond 4 m·s⁻¹. Thus, we defined 4 m·s⁻¹ as the critical velocity.

The mass loss rate is well known to exhibit an exponential relationship with velocity [19]:

$$M = K \cdot v^j \quad (3)$$

where M is the mass loss rate, v is the velocity, j is the speed index and K is a constant related to the material properties and the speed index (e.g., K is 1.81445 when j is equal to 0.77826). To elucidate the relationship between the mass loss rate and velocity, the experimental results were fitted by Eq. (4); the fitting results are presented in Fig. 5. Curve 1

represents the fitting results within the velocity range from 1 to 4 m·s⁻¹. Curve 2 represents the fitting results within the velocity range from 4 to 8 m·s⁻¹. Curve 3 is the fitting results within the velocity range from 1 to 8 m·s⁻¹.

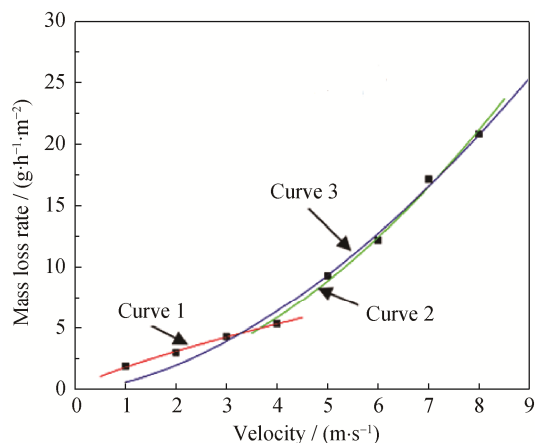


Fig. 5. Mass loss rate curves obtained by fitting experimental data in various ranges of flow velocities: curve 1 (1–4 m·s⁻¹), curve 2 (4–8 m·s⁻¹), and curve 3 (1–8 m·s⁻¹).

The correlation coefficients for curves 1 and 2 were 0.99700 and 0.99348, respectively, demonstrating high mutual reliability. Also, the correlation coefficient for curve 3 was 0.98417. Curve 1 increased gently, whereas curve 2 increased rapidly. These two curves intersected at approximately 4 m·s⁻¹, consistent with the conclusion that the critical velocity is 4 m·s⁻¹.

The morphology of samples after the erosion–corrosion for 2 h at various flow velocities was obtained to reveal the effect of velocity on the damage caused onto the samples, as presented in Fig. 6.

At a flow velocity of 0 m·s⁻¹ (Fig. 6(a)), no erosion trace was observed. The α and γ phases were clearly observed, demonstrating a smooth surface. These effects are explained by the sand and samples being relatively static in the absence of the impinging impact. In the flow velocity range from 1 to 3 m·s⁻¹ (Figs. 6(b)–6(d)), the velocities were still less than the critical velocity. The impact of sand on the sample surface was so weak that only a few scour pits were observed on the surface; furrows were observed in the pits with a preferred direction. The α and γ phases were barely visible on the surfaces, and the surface damage was minor. When the velocity was increased to 4 m·s⁻¹ (Fig. 6(e)), the damage deteriorated. Erosion pits and migration metal lips, along with small holes with material loss, were observed on the specimen surface. Certain small river patterns were observed, whereas the phase boundaries between the α and γ phases became fuzzy. When the

velocity was $5\text{--}6\text{ m}\cdot\text{s}^{-1}$ (Figs. 6(f) and 6(g)), which was greater than the critical velocity, plastic deformation occurred. The erosion pits became deep, and the lips became thicker. Large holes were distributed on the surface. The river patterns extended forward and grew substantially. When the velocity was further increased to 7 and $8\text{ m}\cdot\text{s}^{-1}$ (Figs. 6(h) and 6(i)), the erosion pits changed into meteor-impacted shapes. The lips were stacked, intermingling with each other, and an increasing number of large holes appeared. The river-pattern became obvious, and the surface became substantially “crude” in a lacerate shape. This failure of the sample surfaces further confirmed that the

flow velocity of $4\text{ m}\cdot\text{s}^{-1}$ could be determined as the critical velocity.

3.2. Effect of sand content

The erosion–corrosion behavior of the SAF3207 super duplex stainless steel was studied by varying the medium garnet sand content from 2wt% to 11wt% in a 3.5wt% NaCl solution. The velocity was set at $6\text{ m}\cdot\text{s}^{-1}$, higher than the critical velocity, to maintain a stable weightlessness. The testing duration was 2 h. The mass loss rate curve of specimens in solutions with various sand contents is presented in Fig. 7.

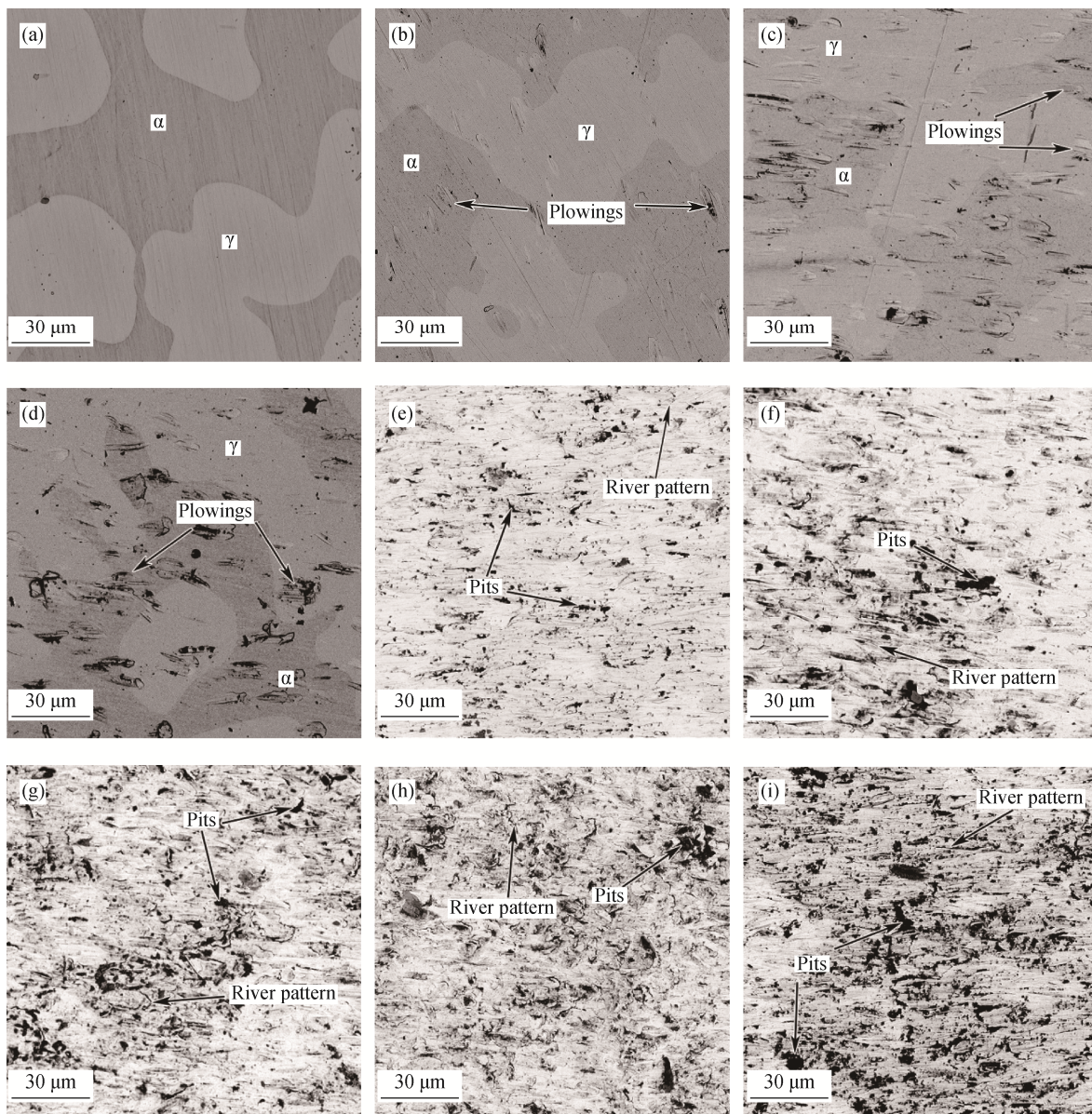


Fig. 6. SEM micrographs of specimens after erosion–corrosion for 2 h at various flow velocities: (a) $0\text{ m}\cdot\text{s}^{-1}$; (b) $1\text{ m}\cdot\text{s}^{-1}$; (c) $2\text{ m}\cdot\text{s}^{-1}$; (d) $3\text{ m}\cdot\text{s}^{-1}$; (e) $4\text{ m}\cdot\text{s}^{-1}$; (f) $5\text{ m}\cdot\text{s}^{-1}$; (g) $6\text{ m}\cdot\text{s}^{-1}$; (h) $7\text{ m}\cdot\text{s}^{-1}$; (i) $8\text{ m}\cdot\text{s}^{-1}$.

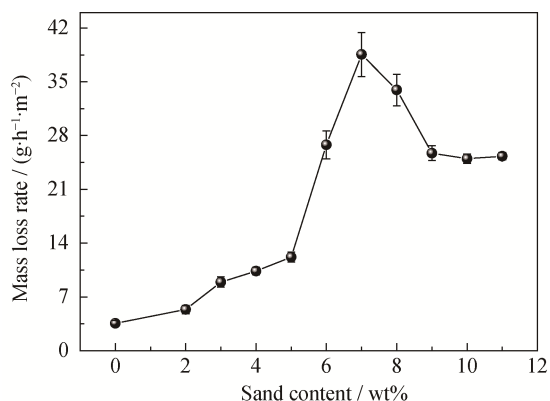


Fig. 7. Mass loss rate curve of specimens in solutions with various sand contents.

The results in Fig. 7 demonstrate that the mass loss rate increased with increasing sand content from 0 to 7wt%, reaching a maximum at 7wt%. The mass loss rate thereafter decreased (7wt%–9wt%) and then tended to remain stable (9wt%–11wt%). When the sand content was increased from 0 to 7wt%, the amount of suspended sand in the solution increased, which amplified the working frequency of the solid particles on the sample surface and, therefore, the mass loss. At 9wt%, the sand content was so high that it decreased the erosion–corrosion rate instead. This change is attributed to two main factors [3,20–21]: First, both the viscosity factor and flow resistance of the solution increased substantially and the turbulence intensity of the solution decreased as the sand content was increased. Moreover, a large number of gas nuclei formed on the sand surface, weakening the cavitation effect. Furthermore, the increase in sand content induced rebound and bumping among the sand particles, thereby reducing the impact on the samples. In the experiments, sand precipitations were observed in the test with a sand content of 9wt%. This observation indicates that the solution could not retain any more sand. The excessive sand covered the sample surface, altering the flow state. Similarly, the 7wt% sand content was defined as the “critical sand content” [22]. The polarization curves of the specimens in the solution with various sand contents (2wt%–11wt%) are presented in Fig. 8 with a velocity of $6 \text{ m} \cdot \text{s}^{-1}$.

In Fig. 8, all of the cathode polarization curves demonstrate the same trend. The testing parameters associated with the potentiodynamic curves are presented in Table 3.

The results show that the passive current density I_p increased as the sand content increased, whereas the passive current density I_p reached a maximum at a sand content of 7wt%. The passive current density I_p decreased to a certain extent when the sand content was increased from 7wt% to 9wt%. Because the sand content exceeded the critical sand

content, the turbulence of the water flow could decrease; simultaneously, the sand had a “shielding effect” on the sample surfaces [23]. These two factors jointly prevented the passivation film from being damaged, thereby reducing the passive current density I_p . However, when the sand content was increased from 9wt% to 11wt%, the impact frequency remained unchanged because of sand precipitation within this range. Therefore, the passive current density I_p changed only slightly.

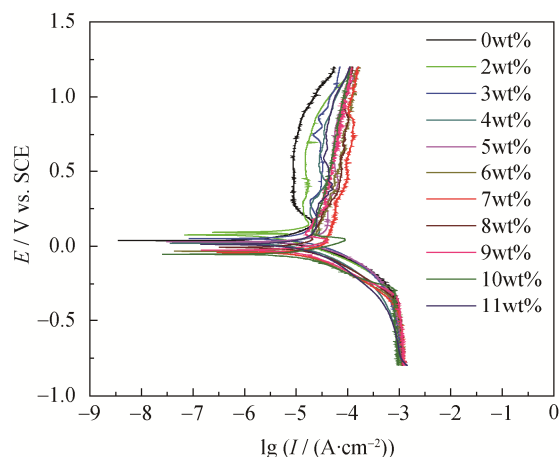


Fig. 8. Polarization curves of specimens in solutions with various sand contents.

Table 3. Test parameters of potentiodynamic curves

Sand content / wt%	$I_p / (\mu\text{A} \cdot \text{cm}^{-2})$	$E_{\text{corr}} / \text{V}$	$I_d / (\mu\text{A} \cdot \text{cm}^{-2})$
0	7.622	0.062	880
2	15.853	0.061	885
3	19.494	0.047	890
4	25.772	0.033	891
5	39.811	0.028	892
6	77.626	-0.016	902
7	98.857	-0.019	910
8	84.693	-0.012	904
9	75.615	-0.011	900
10	74.358	-0.005	899
11	69.444	-0.003	896

Fig. 9 shows the sample morphologies after erosion–corrosion for 2 h under various sand contents. As evident from the results, when the sand content was 0wt%, the sample surface was smooth with no apparent erosion traces, whereas both the α and γ phases were clear and sharp, as presented in Fig. 9(a). As the sand content was increased from 2wt% to 7wt% (Figs. 9(b)–9(g)), the surface damage became increasingly severe. For instance, holes were

formed and became wider and the phase boundaries became fuzzy. In addition, river patterns were observed and the erosion–corrosion pits changed from an isolated state to an intensive distribution in a fish-scale form. When the sand content was increased from 7wt% to 9wt%, the erosion–corrosion damage was diminished and the numbers

of both pits and holes were substantially reduced. The size of the holes decreased, whereas the river patterns became blurry, as presented in Figs. 9(h) and 9(i). When the sand content was increased further to 11wt%, no apparent changes were observed on the surface (Figs. 9(j) and 9(k)).

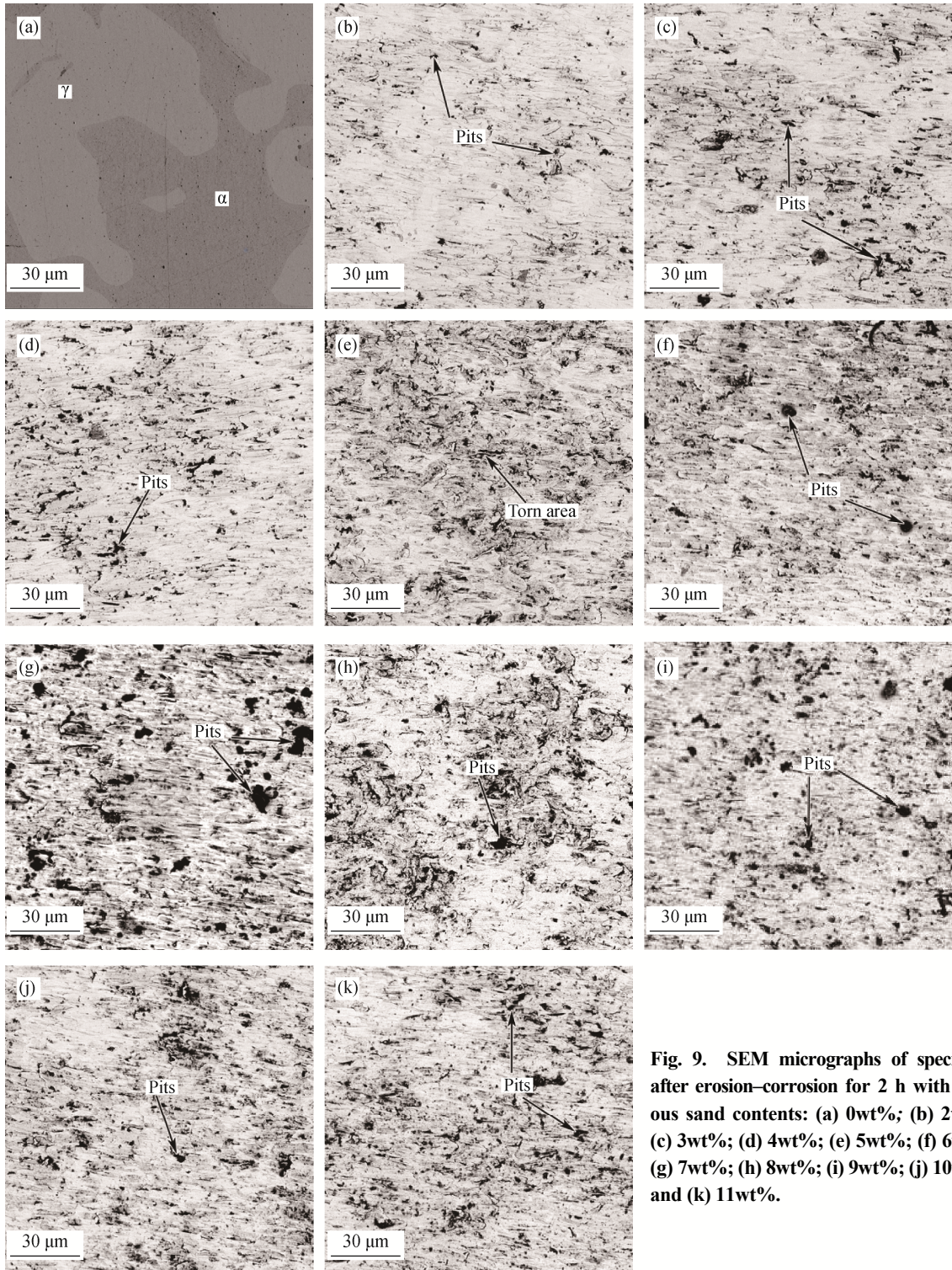


Fig. 9. SEM micrographs of specimens after erosion–corrosion for 2 h with various sand contents: (a) 0wt%; (b) 2wt%; (c) 3wt%; (d) 4wt%; (e) 5wt%; (f) 6wt%; (g) 7wt%; (h) 8wt%; (i) 9wt%; (j) 10wt%; and (k) 11wt%.

The aforementioned analysis indicated that the surface damage demonstrated the same alteration trend with the surface damage of the mass loss. At a sand content of 7wt%, the erosion–corrosion damage was the most severe, as confirmed by our observation that this sample exhibited the greatest number of pits and the widest holes on its surface. This further validated 7wt% as the critical sand content.

3.3. Effect of the testing time

The SAF3207 hyper-duplex stainless steel was tested in a 3.5wt% NaCl solution with 5wt% sand content. The velocity was $6 \text{ m}\cdot\text{s}^{-1}$. The interval for the measurement of the mass loss rate was 0.5 h (the total test time is 6.0 h). Both the cumulative erosion mass loss curve and the erosion mass loss rate curve are presented in Fig. 10.

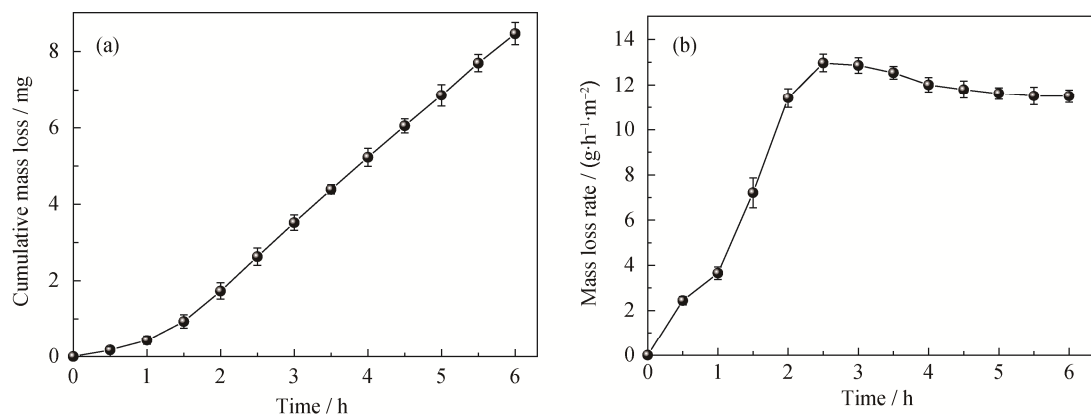


Fig. 10. (a) Cumulative erosion mass loss curve and (b) erosion mass loss rate curve of specimens.

During the sustained period, the cumulative plastic strain reached the critical strain because of the sand-particle repetitive shock. The tested material was removed, and this phenomenon worsened throughout the testing duration. During the stationary period, however, the sample began to enter a stable state and the weightlessness rate was steady in view of the work-hardening and the decreasing ductility.

Many of the previous related studies focused on how the test conditions affected the erosion–corrosion performance rather than on the material changes. To determine the mass loss, we obtained SEM images of the sand before and after erosion; the results are presented in Fig. 11.

In Fig. 11(a), the original garnet sand was observed to exhibit irregular polyhedron shapes with sharp edges and corners. During the incubation period, the sharp edges and corners of the original garnet sand began to disappear (Fig. 11(b)). During the sustained period, these sharp corners became somewhat blunt (Fig. 11(c)) but they still appeared irregular. During the stationary period, both the sharp edges and points were severely polished or blunt (Fig. 11 (d)) and

Fig. 10 shows that the mass loss could be divided into three stages: the incubation period (0 to 1.0 h), the sustained period (1.0 to 2.5 h), and the stationary period (2.5 to 6.0 h). During the incubation period, sample mass loss was not apparent because the mass loss rate was low. As the erosion–corrosion continued, the mass loss entered the sustained period. Both the erosion mass loss and erosion mass loss rate increased, whereas the latter reached a maximum of $12.97 \text{ g}\cdot\text{h}^{-1}\cdot\text{m}^{-2}$ after 2.5 h of erosion processing. The stationary period followed, where the mass loss rate decreased slightly at the beginning and then remained stable at approximately $11.5 \text{ g}\cdot\text{h}^{-1}\cdot\text{m}^{-2}$ after 4 h. During the incubation period [24–25], sand-induced strain occurred. However, the surface of the material had not yet begun to peel off completely because the strain accumulation was insufficient.

most sharp edges and points disappeared as the duration increased (Fig. 11(e)).

The area A and perimeter P of 10 random sand images in the micrographs were calculated using the Image Pro Plus software; the sand shape factor f was thereafter calculated by the following equation:

$$f = 4\pi A/P^2 \quad (5)$$

The average value of the shape factor of the original garnet sand particles was calculated as 0.696, whereas the average values of the shape factors of the incubation period (1 h), the sustained period (2.5 h), and the stationary period (4 h and 6 h) were 0.717, 0.743, 0.812, and 0.819, respectively. These values indicate that, as the erosion time increased, the average shape factor increased gradually. The garnet sand particles became round-shaped because, during the erosion–corrosion, collisions constantly occurred between the sand particles and the samples, as well as between the rebound sand and the slurry jar. These collisions induced a high stress because of the small working area. Ruptures could easily appear on the edges and points because of the

constant erosion–corrosion effect, which would weaken the sand sharpness and consequently reduce the destruction of the surface. At the early stage of the stationary period, the garnet sands were severely blunt, which diminished the destruction of the surface. Therefore, the decrease of the mass loss rate curve at the beginning of the stationary period was

mainly attributed to the low sharpness of the sand.

To explore the erosion behavior and mechanism of materials further, we captured SEM images of the sample surfaces after 20 min of erosion to investigate the erosion–corrosion behaviors in the duplex stainless steels; the images are presented in Fig. 12.

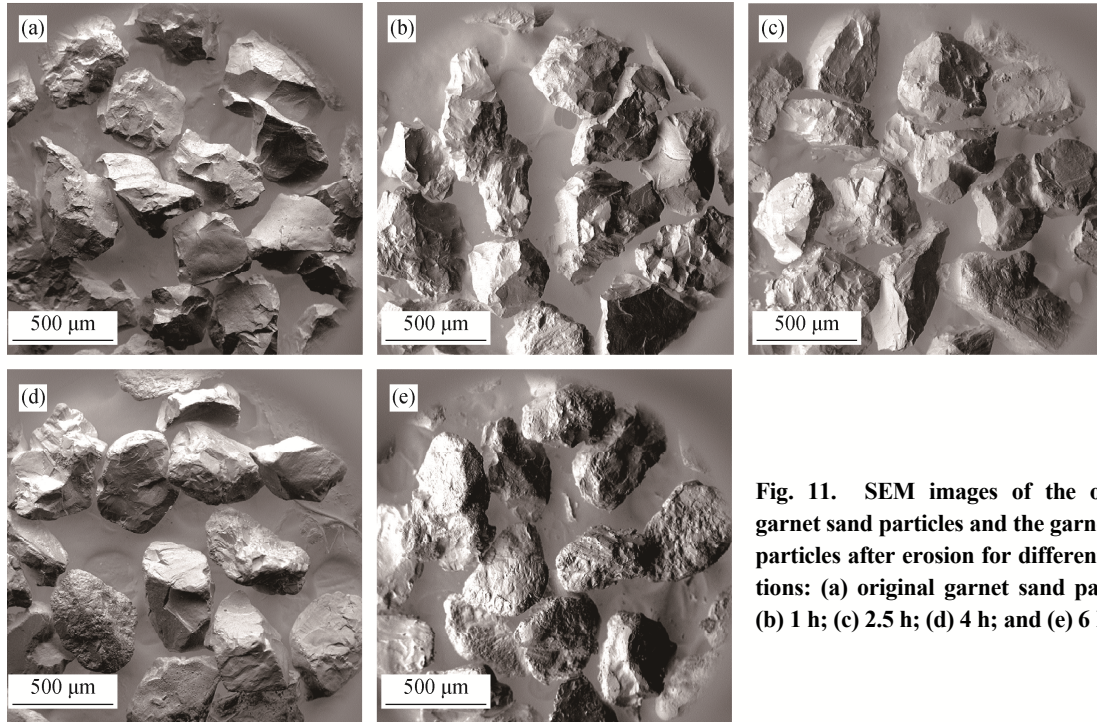


Fig. 11. SEM images of the original garnet sand particles and the garnet sand particles after erosion for different durations: (a) original garnet sand particles; (b) 1 h; (c) 2.5 h; (d) 4 h; and (e) 6 h.

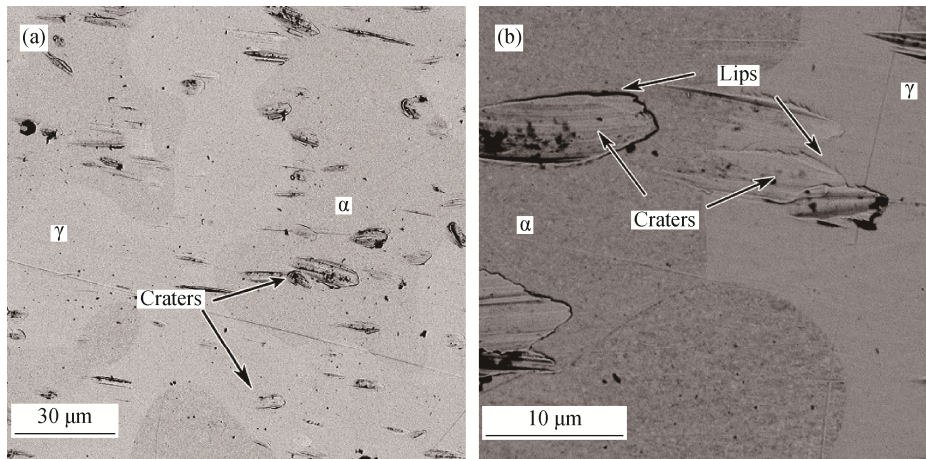


Fig. 12. SEM images of specimens after erosion for 20 min: (a) low magnification and (b) high magnification.

Fig. 12(a) shows that erosion craters formed after the strain deformation induced by the sand particles on the surface. Most craters were distributed in the ferrite phases; only certain craters appeared in the austenite phases. In addition, the erosion craters were apparently orientated because of the low impact angles. The magnified image in Fig. 12(b) shows furrows in the craters, which arose from the sharp

edges and corners of the sand particles. Furthermore, plastic deformation squeezed the erosion craters' volume into the surrounding area, creating extrusion lips. Compared with the austenitic phases, the craters in the ferrite phases were deeper and wider, whereas the extrusion lips were thicker. According to Ref. [26], the anti-erosion property of this material is associated with its hardness. The greater the hard-

ness was, the better the anti-erosion property. Thus, the microhardness of both phases was measured to help explain the aforementioned phenomenon; the hardness of the austenite was HV 365.6, slightly greater than that of the ferrite (HV 344.7). In addition, the austenite has a face-centered structure with a good work-hardening ability. Therefore, in the austenite phases, the craters were small and the lips were thin. In the ferrite phases, on the contrary, the craters were larger and the lips were thicker. During the incubation period, certain plastic deformation occurred on the surface, whereas only a small amount of material loss could be observed.

SEM images of the specimens after erosion for 1 h are presented in Fig. 13. As the erosion duration increased, the surface became rough and blurry. Plastic deformation in both the ferrite and austenite phases was severe. The damage on the ferrite phases was more severe than that on the austenite phases, as presented in Fig. 13(a). A close view of the ferrite area (Fig. 13(b)) demonstrates that the surface was full of craters with orientated furrows. The river-shaped furrows were interconnected. Several chips surrounding the craters exhibited lace-like outer edges. The chips overlapped certain holes and cracks. On the contrary, the austenite zone (Fig. 13(c)) was “smooth” and very few holes and cracks

were observed. Shallow and long river-shaped furrows were also observed in the austenite area. Moreover, the plastic deformation turned the craters into “bands.” As the duration increased, these thick lips on the ferrite were shattered into chips as a result of the continuous sand bombardment.

The cracks formed while the chips became increasingly thinner as the shattering continued. Small chips began to peel off when the cracks propagated. The erosion craters in the austenite area were relatively shallow, whereas the lips were thin, with low ductility; consequently, the lips were squeezed into “bands” instead of chips. During this period, the damage on the ferrite area primarily explains the mass loss, whereas the mass loss on the austenitic area was so low that it suppressed the erosion–corrosion damage to a certain extent, thus resulting in a low total mass loss rate.

SEM micrographs of a specimen after erosion for 3.5 h are presented in Fig. 14. The continuous erosion aggravated the damage on the surface; the surface was rougher and obviously honeycomb-like. In the ferrite area in Fig. 14(b), the chips were reduced compared with those in the area in Fig. 13(b). Also, the holes became wider and deeper, and certain holes even became interconnected, indicating a lamellar tearing mode.

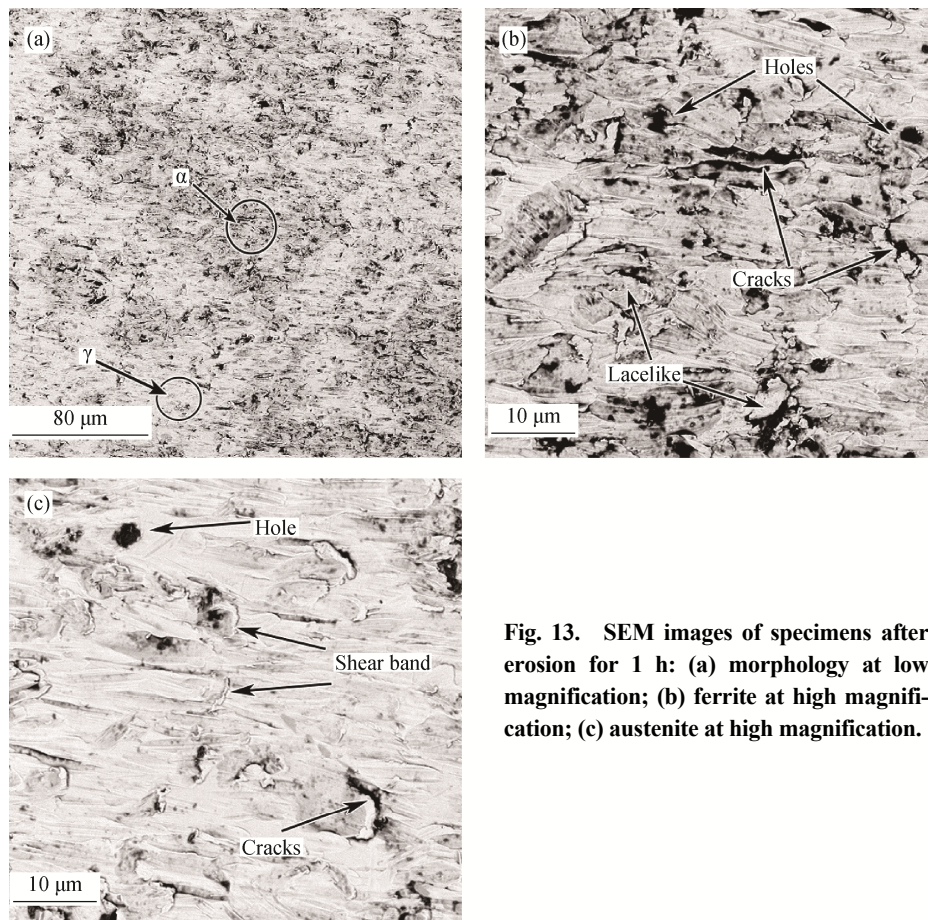


Fig. 13. SEM images of specimens after erosion for 1 h: (a) morphology at low magnification; (b) ferrite at high magnification; (c) austenite at high magnification.

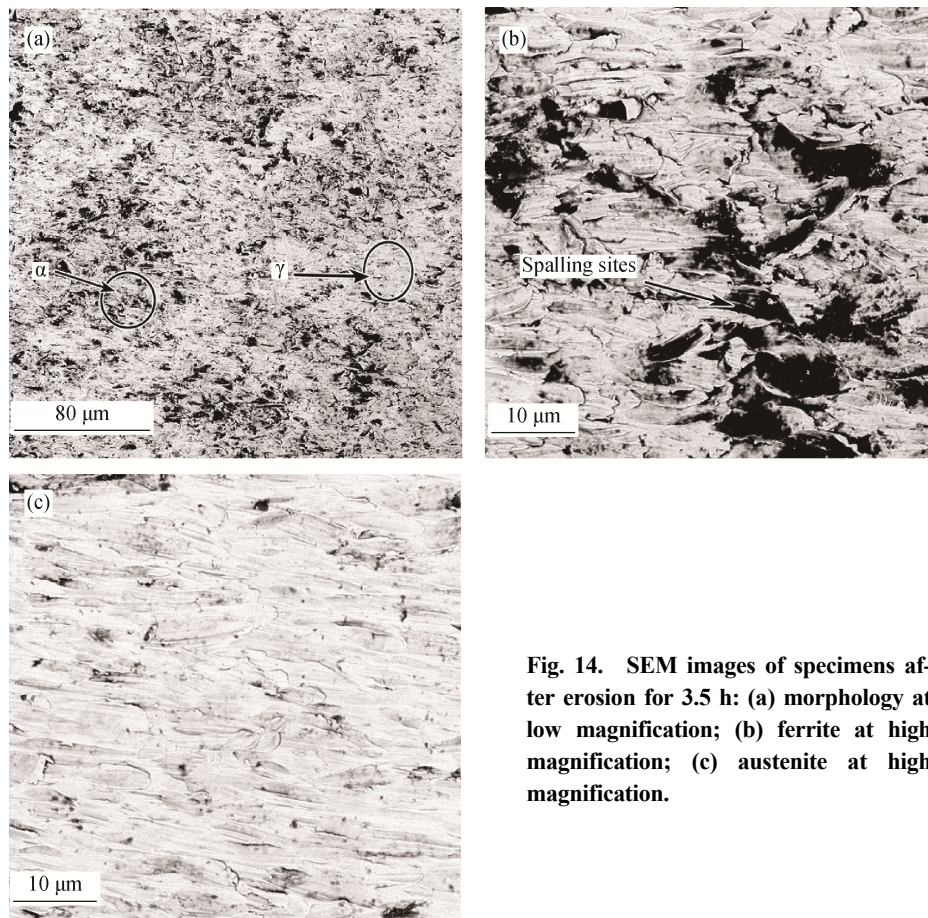


Fig. 14. SEM images of specimens after erosion for 3.5 h: (a) morphology at low magnification; (b) ferrite at high magnification; (c) austenite at high magnification.

Both the mass loss and plastic flow of the material led to the disappearance of river-shaped furrows. In the austenite zone (Fig. 14(c)), the “band” clumps and furrows become shallow. The morphology is smoother than that observed in Fig. 13. In terms of the ferrite area, a high number of chips and cracks existed during the sustained period. As the erosion duration increased, both the role of corrosion dissolution and the impact weakened the impact resistance of the crack region. Therefore, the cracks extended, inducing a smaller connection between the chips and the matrix. Eventually, the chips were removed from the ferrite area. Furthermore, these removed chips accelerated the loss of other chips because of the removal of the support. In the case of the austenite area, on the one hand, austenite could not easily trigger further deformation because of the work-hardening caused by the continuous impingement with the sand; on the other hand, the sand was blunted during this period, and this reduced the damage on the austenite area. In addition, with the interaction of both the sand impact and the anodic dissolution, the “bands” induced by high-speed extrusion during the sustained period were shattered along the shear bands, which appeared at the root of the bands and was consequently removed from the surface. These effects resulted in a smooth

surface of the austenite area, whereas the mass loss rate obviously increased and tended to be consequently stable.

4. Conclusions

The erosion–corrosion behavior of SAF3207 hyper-duplex stainless steel was studied under various testing conditions. On the basis of the aforementioned analysis, the following conclusions were drawn.

(1) The increase in the sand velocity undermined the passivation properties, thus aggravating the electrochemical corrosion. The erosion–corrosion-induced damage to the samples increased substantially when the flow velocity exceeded the critical velocity of approximately $4 \text{ m}\cdot\text{s}^{-1}$.

(2) The mass loss rate increased with an increase in sand content from 0 to 7wt%. Also, the mass loss rate reached the maximum value, and the electrochemical corrosion damage became the most severe when the sand content reached 7wt%. The mass loss rate decreased and became stable when the sand content exceeded 7wt%.

(3) The material mass loss was divided into the incubation, sustained, and the stationary periods. Moreover, the material mass loss rate reached a maximum of $12.97 \text{ g}\cdot\text{h}^{-1}\cdot\text{m}^{-2}$ when the

sample was eroded for 2.5 h. The degradation of the ferrite phases was the main reason for the material mass loss.

(4) The failure modes in both phases of the material differed during the erosion process: both the shallow erosion pits and thin squeeze lips were formed in the austenite area at the beginning of the process. As the erosion–corrosion continued, the thin lips developed into bands with certain microholes and cracks until shear fracture finally occurred along the bands. In the ferrite area, however, the deep pits and thick lips were formed first and consequently were deformed into chips by the sand with a certain amount of cracks, whereas certain chips were developed into tiny holes. As the erosion effect was sustained, the cracks grew substantially and the chips were eventually removed, leaving large holes on the surface.

Acknowledgements

This work was supported by the Major Special Program of Fujian Province, China (No. 2017HZ0001-2), the Joint Innovative Project for Industrial Technology of Fujian Province, China (No. FG-2016001), the Special Funds for Marine High-Tech Industry Development of the Fujian Province of China (High-Tech of Ocean and Fisheries of Fujian Province 2014 No. 14) and the Scientific Research Projects for Young Teachers of Education Department of Fujian Province, China (No. JAT160066).

References

- [1] A.M. Rashidi, M. Packnezhad, M. Moshrefi-Torbati, and F.C. Walsh, Erosion–corrosion synergism in an alumina/sea water nanofluid, *Microfluid. Nanofluid.*, 17(2014), No. 1, p. 225.
- [2] M.A.L. Hernández-Rodríguez, D. Martínez-Delgado, R. González, A. Pérez Unzueta, R.D. Mercado-Solis, and J. Rodríguez, Corrosive wear failure analysis in a natural gas pipeline, *Wear*, 263(2007), No. 1-6, p. 567.
- [3] H. Meng, X. Hu, and A. Neville, A systematic erosion–corrosion study of two stainless steels in marine conditions via experimental design, *Wear*, 263(2007), No. 1-6, p. 355.
- [4] L. Wei, Q.H. Zhao, and S.Z. Li, Relationship between the specific surface area of rust and the electrochemical behavior of rusted steel in a wet–dry acid corrosion environment, *Int. J. Miner. Metall. Mater.*, 24(2017), No. 1, p. 55.
- [5] M.A. Islam and Z.N. Farhat, The synergistic effect between erosion and corrosion of API pipeline in CO₂ and saline medium, *Tribol. Int.*, 68(2013), p. 26.
- [6] J.J. Shi and J. Ming, Influence of mill scale and rust layer on the corrosion resistance of low-alloy steel in simulated concrete pore solution, *Int. J. Miner. Metall. Mater.*, 24(2017), No. 1, p. 64.
- [7] J. Zhu, Q.B. Zhang, Y. Chen, Z. Zhang, J.Q. Zhang, and C.N. Cao, Progress of study on erosion-corrosion, *J. Chin. Soc. Corros. Prot.*, 34(2014), No. 3, p. 199.
- [8] I. Weibull, Duplex stainless steels and their application, particularly in centrifugal separators. Part A, History & Development, *Mater. Des.*, 8(1987), No. 1, p. 35.
- [9] X. Gu, H.L. Xiang, Q.M. Lu, and Y.X. Wang, Effect of solution temperature on the microstructure and corrosion resistant of hyper duplex stainless steel, *Spec. Cast. Nonferrous Alloys*, 33(2013), No. 10, p. 899.
- [10] F.S. He, H.L. Xiang, X. Gu, and D. Lu, Cavitation erosion behavior of Cr₃₂Ni₇Mo₃N super duplex stainless steel, *J. Univ. Sci. Technol. Beijing*, 36(2014), No. 8, p. 1060.
- [11] H.C. Tian, X.Q. Cheng, Y. Wang, C.F. Dong, and X.G. Li, Effect of Mo on interaction between α/γ phases of duplex stainless steel, *Electrochim. Acta*, 267(2018), p. 255.
- [12] B.M. Wei, *Corrosion Theory and Application of Metals*, Chemical Industry Press, Beijing, 1984, p. 55.
- [13] Y.L. Cheng, *Study of the Electrochemical Properties of the Corrosion of Aluminum Alloys in Neutral Sodium and Thin Electrolyte Layers* [Dissertation], Zhejiang University, Zhejiang, 2003, p. 69.
- [14] H.L. Xiang, J.C. Fan, D. Liu, and X. Gu, Effects of antibacterial aging treatment on microstructure and properties of copper-containing duplex stainless steel II. Corrosion resistance and antibacterial properties, *Acta. Metall. Sin.*, 48(2012), No. 9, p. 1089.
- [15] J.T. Huang, *Theory and Application of Cavitation and Cavitation Erosion*, Tsinghua University Press, Beijing, 1991, p. 113.
- [16] E.A.M. Hussain and M.J. Robinson, Erosion–corrosion of 2205 duplex stainless steel in flowing seawater containing sand particles, *Corros. Sci.*, 49(2007), No. 4, p. 1737.
- [17] Y.G. Zheng, Z.M. Yao, K. Long, S.C. Li, and W. Ke, The development of liquid/solid two phase flow erosion experiment device and dynamic electrochemical test, *Corros. Sci. Prot. Tech.*, 5(1993), No. 4, p. 286.
- [18] X.Y. Yong, Y.Z. Lin, J.J. Liu, and S.J. Liu, Erosion corrosion of duplex stainless steel in flowing neutral chloride containing sand, *Acta. Metall. Sin.*, 37(2001), No. 7, p. 745.
- [19] X.X. Jiang, S.Z. Li, S. Li, *Corrosive Wear of Metals*, Chemical Industry Press, Beijing, 2002, p. 113.
- [20] M. Papini, D. Ciampini, T. Krajac, and J.K. Spelt, Computer modelling of interference effects in erosion testing: Effect of plume shape, *Wear*, 255(2003), No. 1-6, p. 85.
- [21] A. Neville, F. Reza, S. Chioveli, and T. Revega, Erosion–corrosion behaviour of WC-based MMCs in liquid–solid slurries, *Wear*, 259(2005), No. 1-6, p. 181.
- [22] Y.G. Zheng, H. Yu, S.L. Jian, and Z.M. Yao, Effect of the sea mud on erosion–corrosion behaviors of carbon steel and low alloy steel in 2.4% NaCl solution, *Wear*, 264(2008), No. 11-12, p. 1051.
- [23] J.S. Sun, *Wear of Metals*, Metallurgical Industry Press, Beijing, 1992, p. 450.
- [24] W. Liu, Y.G. Zheng, Z.M. Yao, X.Q. Wu, and W. Ke, Cavitation erosion of 20SiMn and 0Cr13Ni5Mo steels in distilled water with and without sand, *Acta. Metall. Sin.*, 37(2001), No. 2, p. 197.
- [25] Z.B. Zheng, Y.G. Zheng, W.H. Sun, and J.Q. Wang, Erosion–corrosion of HVOF-sprayed Fe-based amorphous metallic coating under impingement by a sand-containing NaCl solution, *Corros. Sci.*, 76(2013), p. 337.